ISSN 1674-1056
http://cpb.iphy.ac.cn
http://iopscience.iop.org/cpb
中国物理 B
Chinese Physics
中国物理
Chinese Physics B

Photodetectors based on small-molecule organic semiconductor crystals

Jing Pan(潘京), Wei Deng(邓巍), Xiuzhen Xu(徐秀真), Tianhao Jiang(姜天昊), Xiujuan Zhang(张秀娟), Jiansheng Jie(揭建胜)

Citation: Chin. Phys. B . 2019, 28(3): 038102. **doi:** 10.1088/1674-1056/28/3/038102
Journal homepage: http://cpb.iphy.ac.cn; http://iopscience.iop.org/cpb

What follows is a list of articles you may be interested in

Short-wave infrared InGaAs photodetectors and focal plane arrays

Yong-Gang Zhang(张永刚), Yi Gu(顾溢), Xiu-Mei Shao(邵秀梅), Xue Li(李雪), Hai-Mei Gong(龚海梅), Jia-Xiong Fang(方家熊)

Chin. Phys. B . 2018, 27(12): 128102. **doi:** 10.1088/1674-1056/27/12/128102

Photon-counting chirped amplitude modulation lidar system using superconducting nanowire single-photon detector at 1550-nm wavelength

Hui Zhou(周慧), Yu-Hao He(何宇昊), Chao-Lin Lü(吕超林), Li-Xing You(尤立星), Zhao-Hui Li(李召辉), Guang Wu(吴光), Wei-Jun Zhang(张伟君), Lu Zhang(张露), Xiao-Yu Liu(刘晓宇), Xiao-Yan Yang(杨晓燕), Zhen Wang(王镇)

Chin. Phys. B . 2018, 27(1): 018501. **doi:** 10.1088/1674-1056/27/1/018501

Electronic mobility in the high-carrier-density limit ofion gel gated IDTBT thin film transistors

Bao Bei, Shao Xian-Yi, Tan Lu, Wang Wen-He, Wu Yue-Shen, Wen Li-Bin, Zhao Jia-Qing, Tang Wei, Zhang Wei-Min, Guo Xiao-Jun, Wang Shun, Liu Ying

Chin. Phys. B . 2015, 24(9): 098103. **doi:** 10.1088/1674-1056/24/9/098103

The basis of organic spintronics：Fabrication of organic spin valves

Chen Bin-Bin, Jiang Sheng-Wei, Ding Hai-Feng, Jiang Zheng-Sheng, Wu Di

Chin. Phys. B . 2014, 23(1): 018104. **doi:** 10.1088/1674-1056/23/1/018104

Aluminium phthalocyanine chloride thin films for temperature sensing

Muhammad Tariq Saeed Chani, Abdullah M. Asiri, Kh. S. Karimov, Atif Khan Niaz, Sher Bhadar Khan, Khalid. A. Alamry

Chin. Phys. B . 2013, 22(11): 118101. **doi:** 10.1088/1674-1056/22/11/118101

TOPICAL REVIEW — Photodetector: Materials, physics, and applications

Photodetectors based on small-molecule organic semiconductor crystals*

Jing Pan(潘京), Wei Deng(邓巍), Xiuzhen Xu(徐秀真), Tianhao Jiang(姜天昊), Xiujuan Zhang(张秀娟)†, and Jiansheng Jie(揭建胜)‡

Institute of Functional Nano and Soft Materials (FUNSOM), Jiangsu Key Laboratory for Carbon-Based Functional Materials and Devices, Soochow University, Suzhou 215123, *China*

(Received 12 October 2018; revised manuscript received 26 November 2018; published online 25 February 2019)

Small-molecule organic semiconductor crystals (SMOSCs) combine broadband light absorption (ultraviolet–visible–near infrared) with long exciton diffusion length and high charge carrier mobility. Therefore, they are promising candidates for realizing high-performance photodetectors. Here, after a brief resume of photodetector performance parameters and operation mechanisms, we review the recent advancements in application of SMOSCs as photodetectors, including photoconductors, phototransistors, and photodiodes. More importantly, the SMOSC-based photodetectors are further categorized according to their detection regions that cover a wide range from ultraviolet to near infrared. Finally, challenges and outlooks of SMOSC-based photodetectors are provided.

Keywords: small molecule, organic semiconductor crystals, photodetectors

PACS: 81.05.Fb, 81.10.–h, 85.60.Gz, 85.60.Dw **DOI:** 10.1088/1674-1056/28/3/038102

1. Introduction

Small-molecule organic semiconductor crystals (SMOSCs) have become one of the research hotspots in recent years due to their unique optical and electrical properties. Compared with organic thin films, SMOSCs possess fewer grain boundaries, fewer undesirable defects, and long-range-order molecular packing. Thus, they have many distinct advantages, including longer exciton diffusion lengths and higher charge carrier mobilities, which can largely suppress the recombination of excitons and accelerate charge transport.[1] Up to now, SMOSCs have been widely used for realizing high-performance organic light-emitting diodes (OLEDs), organic field-effect transistors (OFETs), organic photovoltaics (OPVs), and organic photodetectors.[2–6]

Spectral response of SMOSCs can also be readily tuned from ultraviolet (UV) to the near infrared (NIR) region by controlling the molecular structure.[5,6] This has enabled the successful development of high-performance and panchromatic photodetectors that are targeted for image sensing and scanners.[7] Moreover, SMOSCs have excellent compatibility with solution-processed methods and flexible substrates, making them possible to realize innovative applications such as implantable optical communication, electronic eye, portable analyzer, and so on.[6–8] Over the past decades, rapid developments in photodetectors based on SMOSCs have been achieved. For example, Schwab *et al.*[9] gave the first demonstration of single-crystalline porphine nanorod-based photodetectors in 2004. Encouraged by their interesting discovery, highly sensitive, low-cost, and flexible photodetectors have been widely investigated by using SMOSCs as light harvesting materials. In addition, benefiting from the development of aligned/patterned strategies, integrated SMOSC-based photodetectors for image sensing applications have been successfully demonstrated.[10] However, no study has yet presented a comprehensive overview of the development and progress for SMOSC-based photodetectors.

Herein, after reviewing the fundamentals and key figure-of-merit parameters of photodetectors in Section 2, we review recent advancements in SMOSC-based photodetectors in Section 3. Three types of photodetectors based on SMOSCs are summarized and discussed in detail. Finally, challenges and outlooks of SMOSC-based photodetectors will be highlighted.

2. Performance characterization and operation principles of SMOSC-based photodetectors

Photodetectors are typical optoelectronic devices that can detect light signals via the photoelectric effect.[11] In this section, the key figures of merit used to characterize photodetectors and most widely adopted device architectures of SMOSC-based photodetectors are summarized.

*Project supported by the National Natural Science Foundation of China (Grant Nos. 51672180, 51622306, and 21673151), Collaborative Innovation Center of Suzhou Nano Science & Technology, the Priority Academic Program Development of Jiangsu Higher Education Institutions (PAPD), the 111 Project, Joint International Research Laboratory of Carbon-Based Functional Materials and Devices.

†Corresponding author. E-mail: xjzhang@suda.edu.cn

‡Corresponding author. E-mail: jsjie@suda.edu.cn

© 2019 Chinese Physical Society and IOP Publishing Ltd

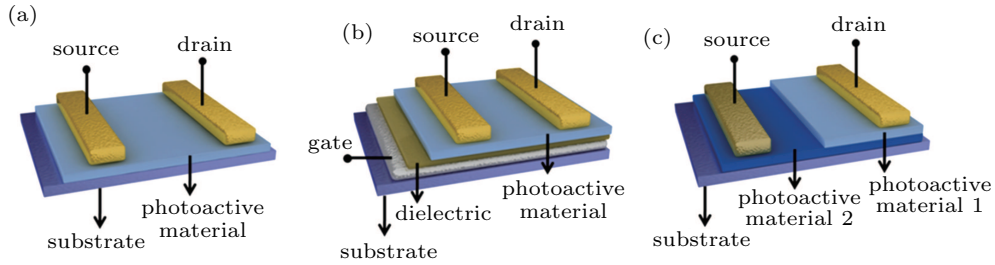


Fig. 1. Schematic diagrams of three typical photodetector structures: (a) photoconductor, (b) phototransistor, and (c) photodiode.

2.1. Basic parameters

External quantum efficiency (EQE): EQE is the ratio of the number of photo-generated carriers to the number of incident photon. It can be expressed as

$$\mathrm{EQE} = \frac{I_{\mathrm{ph}}/q}{P_{\mathrm{in}}/h\nu}, \tag{1}$$

where I_{ph} is the photocurrent, q is the elementary charge, P_{in} is the incident light power, h is the Planck constant, and ν is the frequency of the incident light. To achieve a large EQE, the active layer is required to have high optical absorption and few carrier trap states.[12]

Responsivity (R): R is defined as the ratio of photocurrent to incident-light intensity, which is usually expressed as

$$R = \frac{I_{\mathrm{ph}} - I_{\mathrm{dark}}}{P_{\mathrm{in}}}, \tag{2}$$

R is used to indicate how efficiently a photodetector responds to a given incident optical signal. Because R is proportional to the EQE, it can also be expressed as

$$R = \frac{\mathrm{EQE} \cdot \lambda q}{hc}, \tag{3}$$

where I_{dark} is the dark current, λ is the wavelength of the incident light, and c is the speed of light.

Detectivity (D): it is used to describe the ability of weak light detection, the normalized value is called the specific detectivity (D^*), which can be written as

$$D^* = \frac{R\sqrt{AB}}{I_{\mathrm{noise}}}, \tag{4}$$

where I_{noise} is the total noise current, A and B are the working area and bandwidth of the device, respectively. If the shot noise becomes dominant over the total noise from the dark current,[12] D^* can then be written as

$$D^* = \frac{R\sqrt{A}}{\sqrt{2qI_{\mathrm{dark}}}}, \tag{5}$$

the corresponding terms have been explained above.

Response speed (t): it determines the ability of a photodetector to follow a rapid modulated light signal, which is characterized by the rise time (t_{r}) and fall time (t_{f}). The rise time t_{r} or the fall time t_{f} is defined as the time required for the response to rise from 10% to 90% or to decay from 90% to 10% of the peak value.

2.2. Device architectures and their working mechanisms

According to the working mechanisms, SMOSC-based photodetectors can be categorized as photoconductors, phototransistors, and photodiodes. Photoconductors are typical two-terminal devices (Fig. 1(a)) that utilize the photoconductive effect. They can provide a high EQE and photocurrent gain at the expense of reduced response speed.[6,11] Phototransistors have the same three-terminal configuration of OFETs that use the photogating effect to magnify the photocurrent (Fig. 1(b)). The gate voltage creates a vertical electric field to assist the spatial segregation of photogenerated excitons. For a p-type device, since the lifetime of electrons is larger than the transit time of holes, a few electrons will accumulate in the channel. Extra holes will be injected from electrodes to neutralize the accumulated electrons, resulting in increased photocurrent and a high gain. However, the long lifetime of the electrons will limit the response time of phototransistors. Consequently, phototransistors which show high gain cannot operate at a fast speed. Photodiodes are also two-terminal devices that have sandwich-like structures similar to photovoltaic cells (Fig. 1(c)).[5] However, the most popular topology in SMOSC-based photodiodes is the lateral structure, which uses p- and n-type photoactive materials to construct p–n junction. The significant difference in the work functions of the p- and n-type materials produces a built-in potential, accelerating the exciton dissociation and carrier transport. Thus, compared with photoconductors and phototransistors, photodiodes generally have low dark current, large D^*, and fast response speed.[5]

3. SMOSC-based photodetectors

3.1. SMOSC-based photoconductors

Photoconductor is the simplest type of the three device structures. The photoactive region can generate excitons upon light illumination, which can then dissociate into free charge carriers under an external bias voltage.[6] In the past two decades, studies on the photoconductivity of SMOSCs have developed rapidly. In this section, we will review photoconductors based on SMOSCs for different spectral response regions, ranging from UV to NIR light.

3.1.1. SMOSC-based visible light photoconductors

The preparation of high-quality SMOSCs with appropriate optical bandgap is of significant importance for the realization of high-performance visible photodetectors. Solution-based self-assembly has been frequently adopted for the fabrication of organic single-crystalline nanowires, nanorods, or nanoribbons.[13] Early in 2004, Schwab and coworkers[9] used a simple drop-casting method to prepare meso-tetrakis(4-sulfonatophenyl)porphine nanorods. Upon 488 nm light illumination, the device containing approximately 6100 nanorods showed a rapid response speed of less than 100 ms. Although the photoswitching ratio was not high due to the existence of the charge storage mechanism in the device, this work paved the way for using SMOSCs to realize visible photodetectors. In another example, Jiang *et al.*[14] studied the photoconductive behavior of self-assembled 2-anthracen-9-ylmethylene malononitrile micro-/nanowires (Figs. 2(a) and 2(b)). It was found that the morphology of the as-fabricated one-dimensional (1D) structures has an influence on the absorption spectra (Fig. 2(c)), where the absorption peak was red-shifted with increasing size due to more aggregated molecules narrowing the energy bandgap. A photoswitching ratio of ~ 100 was obtained under white light for the device with multiple microwires (Fig. 2(d)). Also, Zhou *et al.*[15] reported a photoconductive device based on a single benzothiophene sub-micron ribbon (Fig. 2(e)). Since two absorption peaks were found at 414 nm and 387 nm (Fig. 2(f)), photoelectric measurements were thus performed under a violet light of 405 nm. The R was measured to be 420 A·W^{-1} with a photoconductive gain of about 1.3×10^3. Interfacial modification was further used to boost the photodetector performance.[16] As illustrated in Fig. 2(g), a dielectric layer such as poly(methyl methacrylate) (PMMA) or polystyrene (PS) was pre-coated on a quartz substrate before the self-assembly of benzothiophene sub-micron ribbons. It was found that the dielectric/organic crystal interface could influence the surface morphology, polarity, as well as the density of defects. The weak PS dipoles would reduce the defect density and facilitate carrier transport, leading to an enhanced photoconductive gain of 1.3×10^4 and a higher R of 4372 A·W^{-1}, respectively (Fig. 2(h)).

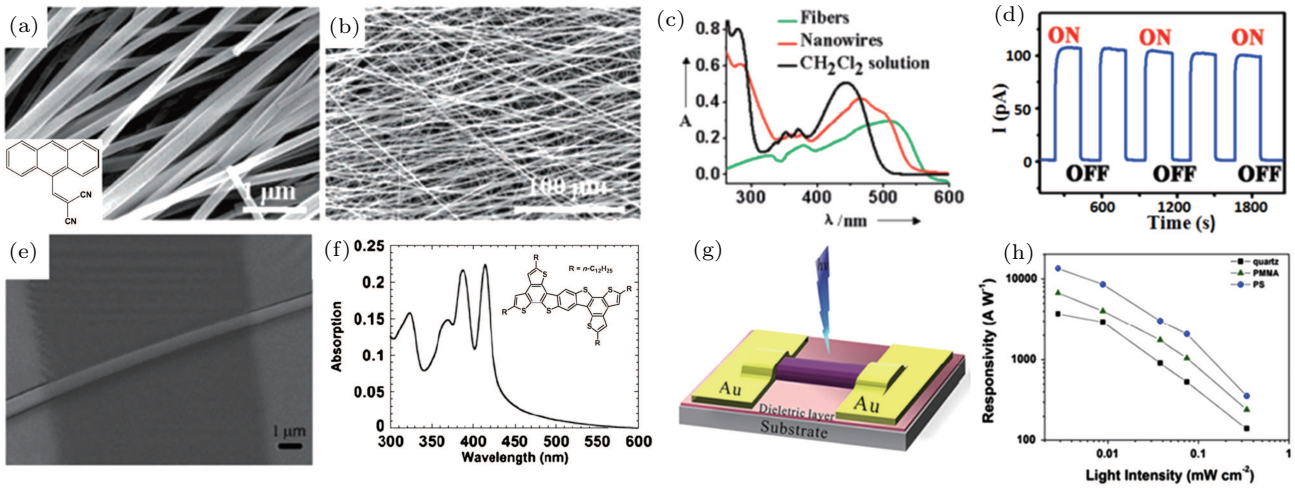


Fig. 2. Scanning electron microscopy (SEM) images of self-assembled 2-anthracen-9-ylmethylene malononitrile (a) nanowires and (b) microwires. (c) Absorption spectra of 2-anthracen-9-ylmethylene malononitrile in solution, nanowire, and microwire phase. (d) Temporal response of the anthracen-based photoconductor under 5 mW·cm^{-2} white light with a bias voltage of 50 V. (a)–(d) Reproduced with permission.[14] Copyright 2008, American Chemical Society. (e) SEM image of a single benzothiophene sub-micron ribbon. (f) Absorption spectrum of benzothiophene sub-micron ribbons. (e), (f) Reproduced with permission.[15] Copyright 2008, Wiley-VCH. (g) Schematic diagram of a single benzothiophene sub-micron ribbon photoconductor. (h) Dependence of the responsivity on the light intensity, the devices are with different dielectric materials. (g), (h) Reproduced with permission.[16] Copyright 2013, Elsevier.

Copper phthalocyanine (CuPc) is another typical small-molecule organic material for red light detection. Due to the outstanding thermal and chemical stability, the CuPc molecules can easily form ordered stacks during a physical vapor deposition (PVD) process. A schematic illustration is shown in Fig. 3(a), where a tube furnace is used for material sublimation and deposition. The CuPc powder source is put in the high-temperature zone, where they are heated above the sublimation point. With the aid of a constant gas flow (usually Ar), CuPc molecules can easily be transported downstream and finally crystallize in the low-temperature zone. Since the whole process is in an isolated system which excludes the influence of ambient air and solvent molecules, highly purified 1D CuPc single crystals can be obtained. A typical case is shown in Fig. 3(b), where ultralong CuPc nanowires up to millimeter in length could grow along the channels of a grating template in a PVD process.[17]

One of the very important advantages of photoconductive devices is that they can be easily integrated for image sensors. Jie *et al.*[18,19] first demonstrated patterning of CuPc

nanowire arrays as image sensors. The patterning of CuPc nanowire arrays was realized by using a metallic nanoparticle-assisted PVD method, as shown in Fig. 3(c). It was found that CuPc nanowires selectively grew on the Au nanoparticle coated areas with an average tilt angle of $\sim 70^{\circ}$ relative to the substrate.[18] By combining the photolithography technique, CuPc nanowires could be patterned in micro-scale pixels.[19] Integrated image sensors with 10×10 pixel arrays in an area of 1.3×1.3 mm^2 were thus fabricated. When the device was exposed to a red laser beam (Fig. 3(d)), the output current intensity mapping gave an accurate sketch of the laser beam shape (Fig. 3(e)). Recently, well aligned organic/inorganic hybrid $CH_3NH_3PbI_3$ single crystals have been reported by Deng *et al.*[20] for visible light (360–780 nm) detection. Flexible and integrated image sensors based on $CH_3NH_3PbI_3$ microwire arrays were constructed on a polyethylene terephthalate (PET) substrate, which showed an excellent image-sensing ability under different bending states (Fig. 3(f)). The novel image sensors can realize high-resolution, broadband and flexible detection at the same time, which are ideal to meet the needs of modern society.

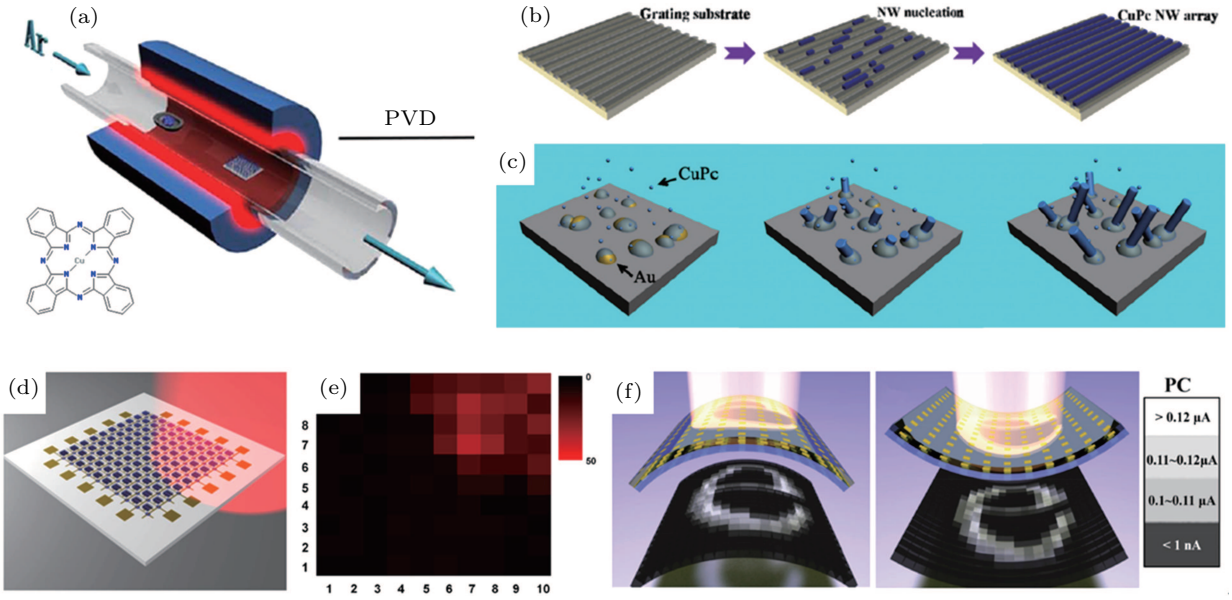


Fig. 3. (a) Schematic illustration of a metallic nanoparticle-assisted PVD process. (b) Template-guided growth of CuPc nanowire arrays. (b) Reproduced with permission.[17] Copyright 2012, The Royal Society of Chemistry. (c) Au-induced growth of cross-aligned CuPc nanowires. (d) Schematic illustration of the measurement configuration for a image sensor: a red laser beam was projected onto the right-upper corner of the device. (e) The corresponding output current intensity mapping of the device. (a), (c)–(e) Reproduced with permission.[19] Copyright 2013, Nature Publishing Group. (f) Schematic illustration of a flexible image sensor based on $CH_3NH_3PbI_3$ microwire arrays. (f) Reproduced with permission.[20] Copyright 2016, Wiley-VCH.

3.1.2. SMOSC-based UV photoconductors

The detection of UV light radiation presents a wide range of civil and military applications, such as flame detection, combustion monitoring, and missile warning.[21] SiC, GaN, and diamond as building blocks for UV photodetectors have attracted intense attention.[22–24] Fabrication of these devices requires costly processes, thus SMOSC-based UV photoconductors in this case provide the opportunity for device fabrication simplification.

Zhang *et al.*[25] demonstrated highly responsive UV photoconductors using ris(8-hydroxyquinoline) aluminum (Alq3) microplates and nanorods. In order to fabricate device, pre-patterned photoresist hollows were constructed by photolithography. With the aid of capillary force and alternating-electric field (Fig. 4(a)), Alq3 microplate (Fig. 4(b)) or nanorods (Fig. 4(c)–4(e)) would selectively deposit in the hollows. UV–Vis absorption spectrum in Fig. 4(f) confirmed that Alq3 has an absorption peak at ~ 250 nm with little absorption in visible light region, which is ideal for pure-UV detection. Photodetectors made from Alq3 single nanorod and microplate were with high R and D^* of 14.5 A·W^{-1}, 19.9×10^{11} Jones and 2.5 A·W^{-1}, 4.24×10^{11} Jones under 254 nm UV light, respectively. More recently, single-crystalline C_{60} microribbon arrays were also adopted for UV photodetectors.[26] The growth process of C_{60} microribbon arrays is illustrated in Fig. 4(g). The SiO_2/Si substrate was first immersed into the C_{60} solution and then lifted up with an optimized speed. Finally, C_{60} single crystals could grow at the contact line along the lifting direction to form ordered arrays (Fig. 4(h)). Current–voltage (I–V) characteristics of C_{60} microribbon arrays were measured in dark and under illumination with different wavelengths ranging from 350 nm to 650 nm (Fig. 4(i)). Prominent current change was observed under UV light illumination, while the device showed slight response to visible light. The photoswitching behavior was further measured under 400 nm light (Fig. 4(j)), and a remarkable photoswitching ratio of 365 was observed at a light intensity of 1.82 mW·cm^{-2}.

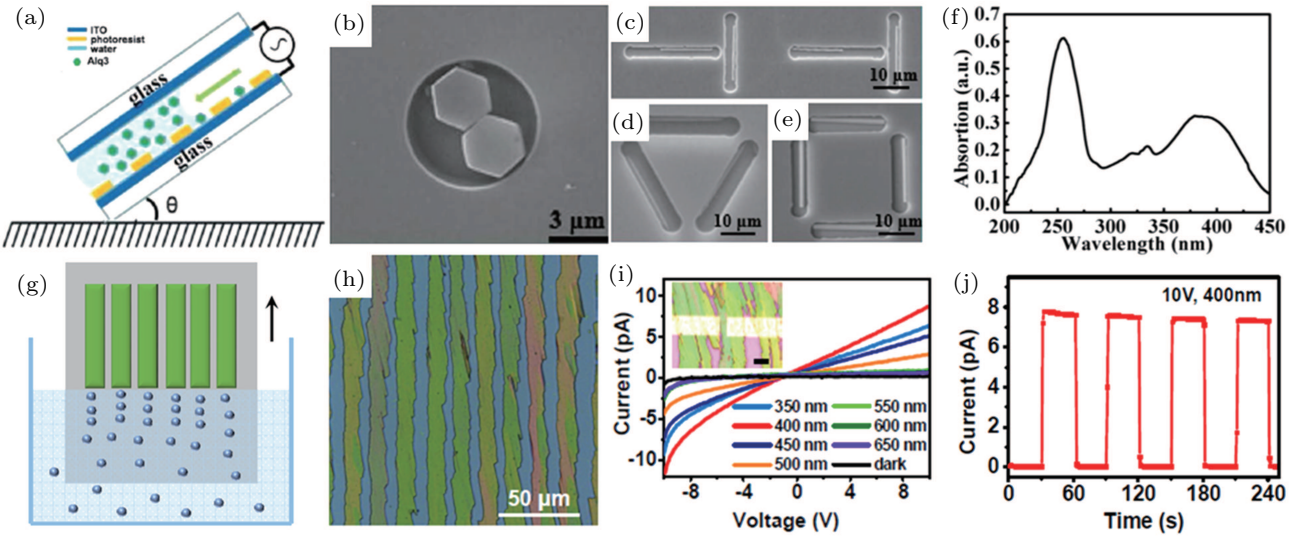


Fig. 4. (a) Schematic illustration of the capillary-assisted alternating electric field method for patterning Alq3 crystals. (b)–(e) SEM images of the as-fabricated Alq3 crystals in different hollows. (f) Absorption spectrum of Alq3 single crystals. (a)–(f) Reproduced with permission.[25] Copyright 2017, Wiley-VCH. (g) Schematic illustration of the dip-coating process for growing C_{60} microribbon arrays. (h) Optical microscopy image of the as-prepared C_{60} microribbon arrays. (i) *I*–*V* characteristics of the C_{60} microribbon arrays under different illumination conditions. Inset: optical microscopy image of a single device. (j) Photoswitching behavior of C_{60} microribbon arrays under 400 nm light with a bias of 10 V. (g)–(j) Reproduced with permission.[26] Copyright 2018, Elsevier.

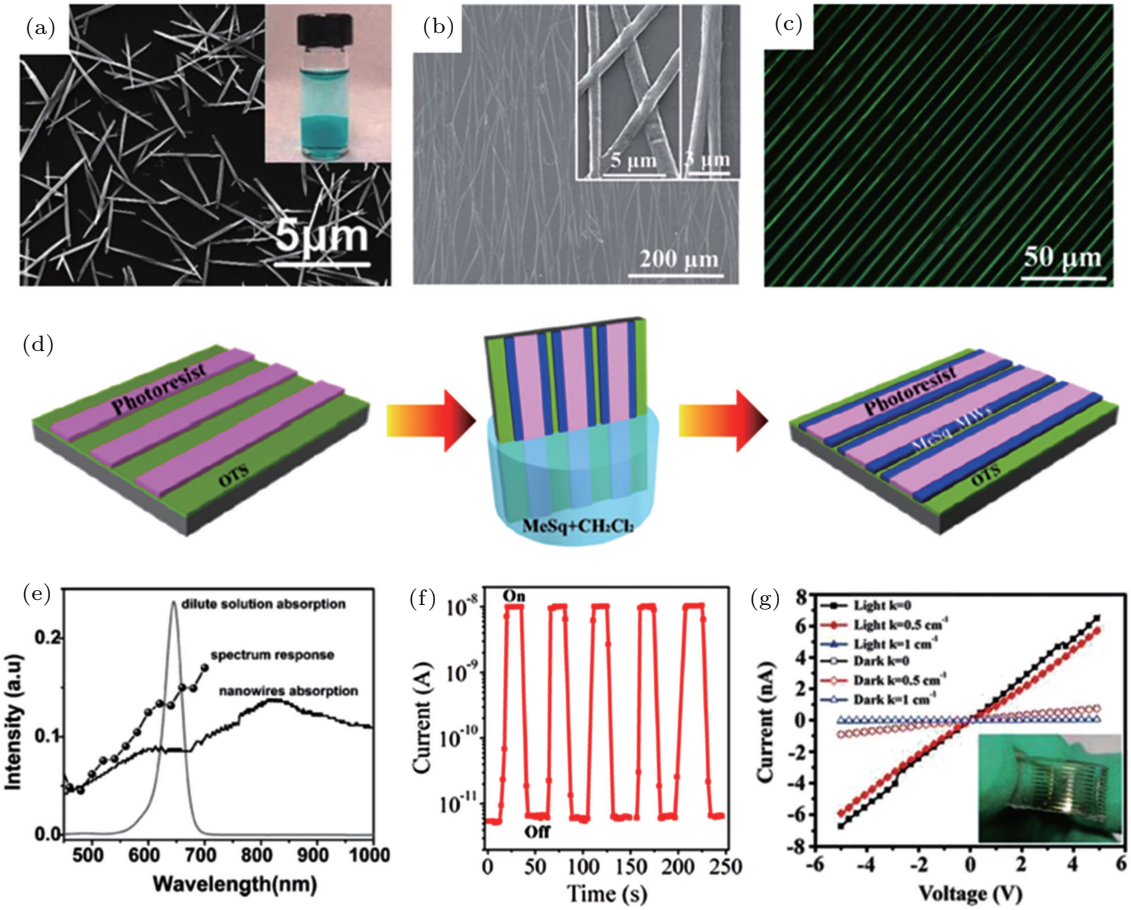


Fig. 5. (a) MeSq nanowires obtained from the solvent exchange self-assembly method. Inset: photography of the precipitation of MeSq nanowires in a glass vial. (b) SEM images of MeSq microwires. (c) Cross-polarized optical microscopy image of the MeSq microwire arrays. (d) Schematic illustration of the patterning strategy for growing MeSq microwire arrays. (e) Absorption spectra of the MeSq nanowires and the MeSq solution with photocurrent spectral response behavior of a single nanowire device. (a), (e) Reproduced with permission.[31] Copyright 2008, Wiley-VCH. (f) Temporal response of the MeSq microwire arrays under 200 mW·cm^{-2} 808 nm light. (c), (d), (f) Reproduced with permission.[33] Copyright 2016, American Chemical Society. (g) *I*–*V* characteristics of a flexible MeSq microwire photoconductor with different curvatures in dark and under 808 nm light irradiation. Inset: photograph of the device on a flexible PDMS substrate. (b), (g) Reproduced with permission.[32] Copyright 2015, American Scientific Publishers.

3.1.3. SMOSC-based NIR photoconductors

NIR photodetectors offer promising applications in passive night vision, optical communication, and biodiagnostics.[27–29] Current inorganic NIR photodetectors are expensive and dependent on costly and complex epitaxial growth on crystalline substrates.[30] Contrastingly, narrow-bandgap SMOSCs offer opportunities for realizing low-cost and flexible NIR photodetectors.

Methyl-squarylium (MeSq) is an ideal organic compound for NIR light harvesting thanks to its good stability and absorption peak in the range of 700–1100 nm. Jie and coworkers reported photoconductors based on 1D MeSq micro-/nanostructures such as nanowires[31] and microwires[32] (Figs. 5(a) and 5(b)) using solution-based methods. Typically, dip-coating was used for ordered alignment of the MeSq microwire arrays,[33] which showed uniform color under cross-polarized light (Fig. 5(c)), demonstrating the single-crystalline nature. The detailed dip-coating process is shown in Fig. 5(d). Photolithography was first used to construct periodic photoresist strips on a SiO_2/Si substrate. Then the exposed areas between wettable photoresist strips were modified by a layer of nonwettable octadecyltrichlorosilane (OTS). Finally, by vertically immersing the patterned substrate into MeSq/dichloromethane (CH_2Cl_2) solution and pulling it up slowly, MeSq microwires would preferentially grow along the bilateral sides of the photoresist stripes. Interestingly, study showed that MeSq/CH_2Cl_2 dilute solution only had a narrow absorption peak in the range of visible light, while the assembled MeSq nanowires had an absorption peak value at around 850 nm (Fig. 5(e)).[31] Therefore, the MeSq microwire arrays were then tested under a 808 nm NIR laser beam. The microwire array device showed pronounced photoresponse under a light intensity of 200 mW·cm^{-2}, with a high photoswitching ratio up to 1600 (Fig. 5(f)). Furthermore, the MeSq microwire could be transferred to a flexible polydimethylsiloxane (PDMS) substrate.[32] The flexible microwire device showed little degradation under 808 nm light upon being bended with bending curvatures (k) increasing from 0.5 cm^{-1} to 1 cm^{-1}, demonstrating the application potential in flexible NIR sensors (Fig. 5(g)). Compared to SMOSC-based visible and UV photoconductors, few examples have been reported in the case of NIR photoconductors. This is mainly because small-bandgap organic semiconductors are too unstable to be synthesized effectively.

3.2. SMOSC-based phototransistors

To date, organic phototransistors (OPTs) have attracted great research interest, because they are able to realize photodetection and signal amplification at the same time. Compared with photoconductive devices, phototransistors can provide significantly higher photoconductive gains with the aid of gate bias. Therefore, they are promising candidates for high-performance photodetectors.[5,6] Here, we will review OPTs based on SMOSCs for different spectral regions, ranging from UV to NIR light.

3.2.1. SMOSC-based visible light phototransistors

First example of SMOSC-based visible light phototransistors was demonstrated by Rovira *et al.* in 2006.[34] Microscale tetrathiafulvalene (TTF) single crystals with a high mobility of 1 cm^2·V^{-1}·s^{-1} were adopted to fabricate OPTs. The OPTs showed a very high photoswitching ratio up to 10^4 at a gate voltage of 10 V under white light (2.5 W·cm^{-2}). In most cases, solution-phase synthesis is preferable for designing well-ordered molecular structures with face-to-face or slip-stacked π–π arrangement, where the strong π–π interaction facilitates the charge transport. For example, 1D 9,10-bis(phenylethynyl)anthracene (BPEA) nanoribbons,[35] 6-methyl-anthra[2,3-b]benzo[d]thiophene (Me-ABT) microribbons,[36] and N,N'-bis(2-phenylethyl)-perylene-3,4:9,10-tetracarboxylic diimide (BPE-PTCDI) nanowires[37] have been fabricated successfully by simple solution-based self-assembly methods. Typically, the Me-ABT-based OPT had a high R of 1.2×10^4 A·W^{-1} under white light, which is comparable to commercial single-crystalline silicon thin film transistors ($\sim$ 300 A·W^{-1}).[38] In terms of charge-transfer complexes, they are often found in organic conjugated polymers, while Zhu's group[39] fabricated two-dimensional (2D) cocrystals successfully. Meso-diphenyltetrathia[22]-annulene[2,1,2,1] (DPTTA) molecules (donors) and C_{60}/C_{70} molecules (acceptors) were segregated to form linear column networks in long-range order (Fig. 6(a)). The as-fabricated C_{70}-DPTTA microsheets have balanced ambipolar properties with an electron mobility of 0.05 cm^2·V^{-1}·s^{-1} and a hole mobility of 0.07 cm^2·V^{-1}·s^{-1}. The enlarged 2D donor–acceptor interfaces facilitated charge separation and provided a highway for charge transport. With the aid of a large gate bias, the C_{70}-DPTTA microsheets have a R of 300 A·W^{-1} under white light (Fig. 6(b)).

For large-scale device application, the capillary tube induced self-assembly was developed to fabricate ordered organic single-crystalline nanowire arrays. As shown in Figs. 6(c), 7,7,8,8-tetracyanoquinodimethane (TCNQ) solution was added drop-wise along a 3-cm-long capillary tube with an outer diameter of 1.2 mm.[40] During continuous baking, the solvent evaporated with meniscus shrinking, which induced the formation of 1D TCNQ crystals (Fig. 6(d)) in directions normal to the tube length. Instead of the traditional Si substrate with SiO_2 gate dielectric, poly(4-vinyl phenol) (CL-PVP) with a high dielectric constant was spin-coated on an indium tin oxide (ITO) substrate. As a result, the output characteristics of TCNQ-based OPTs showed excellent saturation

behavior at low gate and source-drain bias (Fig. 6(e)). The device was capable of low-voltage operation of less than 0.5 V, which was far smaller than the common high gate voltage (V_G) of $\sim$ 20 V. A fast response speed of $\sim$ 10 ms was also observed, as a trade-off, the R was only $\sim$ 1 mA·W^{-1}. Mukherjee *et al.*[41] used the same method to construct OPTs based on N,N'-dioctyl-3,4,9,10-perylenedicarboximide (PTCDI-C8) nanowire arrays, which exhibited a R of 7 A·W^{-1} under 7.5 mW·cm^{-2} white light. Yao *et al.*[42] further utilized CL-PVP as the protective layer in a photolithography process, preventing the downside PTCDI-C8 nanowires from being damaged during photoresist development. Then electrodes with different channel lengths were deposited (Fig. 6(f)), the shortest of which was downscaled to $\sim$ 200 nm. Short channel effect of the PTCDI-C8 nanowire-based OPTs was studied. The normalized photocurrents of different channel lengths were measured under a wavelength range from 320 nm to 690 nm (Fig. 6(g)). For OPTs with the shortest channel length, the photocurrents fit the absorption spectrum best. The temporal response of OPTs with different channel lengths is shown in Fig. 5(h). Devices with narrower channels exhibited higher current both in light on and off state, which was probably due to fewer grain boundaries and fewer trap states in a shorter region. Therefore, the OPTs with short channel lengths revealed a high R up to 4.8×10^4 A·W^{-1}.

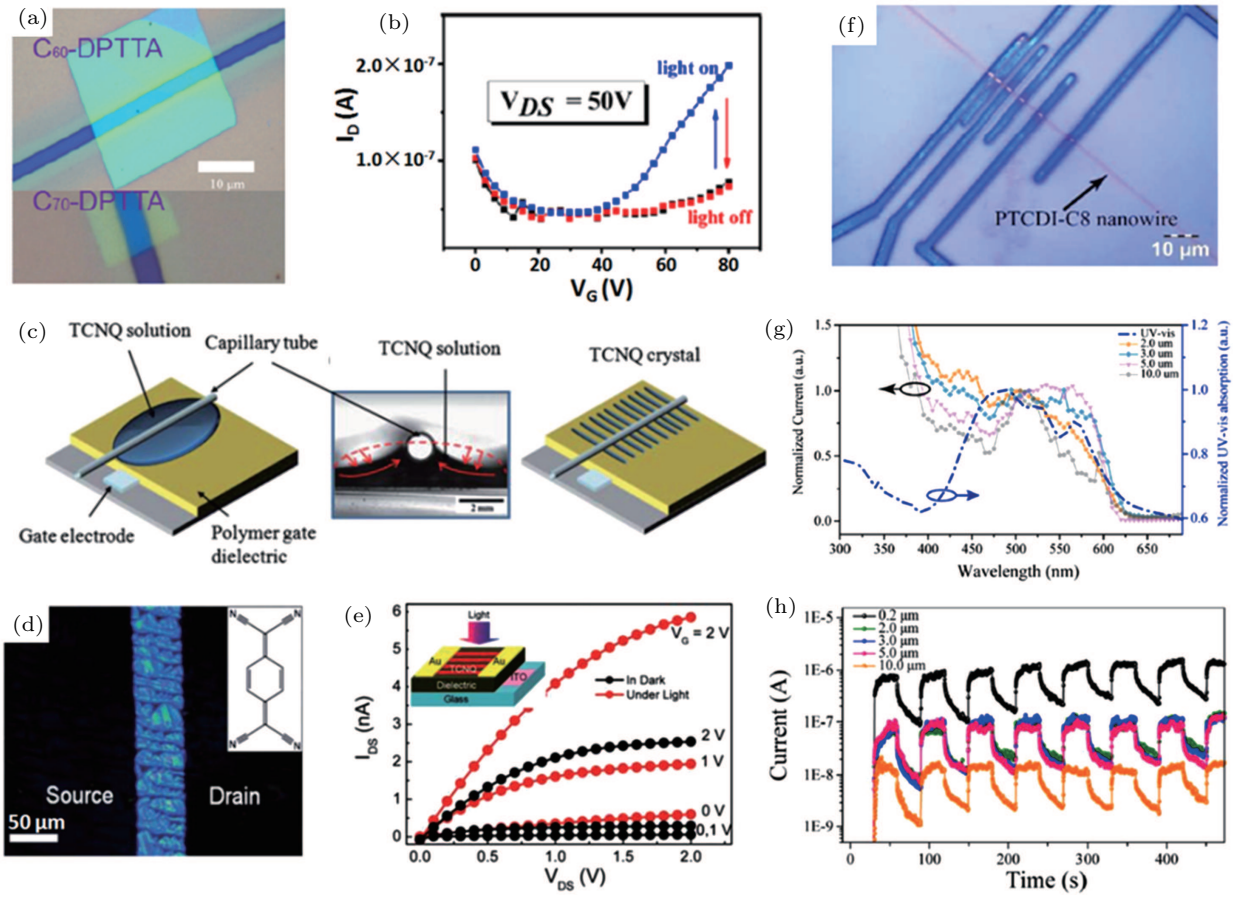


Fig. 6. (a) Optical microscopy images of OPTs based on C_{60}-DPTTA and C_{70}-DPTTA cocrystals. (b) Transfer characteristics of the ambipolar device in dark (red line) and illumination (blue) conditions. (a), (b) Reproduced with permission.[39] Copyright 2013, American Chemical Society. (c) Schematic illustration of the capillary tube induced self-assembly of TCNQ crystals. (d) Optical microscopy image of a TCNQ-based OPT. (e) Output characteristics of a TCNQ-based OPT at low gate and source-drain voltages. (c)–(e) Reproduced with permission.[40] Copyright 2011, The Royal Society of Chemistry. (f) Optical microscopy image of a single PTCDI-C8 nanowire OPT with different channel lengths. (g) The normalized photocurrent spectra of PTCDI-C8-based OPTs with different channel lengths versus the normalized absorption spectra of PTCDI-C8. (h) Temporal response of a single PTCDI-C8 nanowire OPT with different channel lengths under 500 nm light. (f)–(h) Reproduced with permission.[42] Copyright 2018, American Chemical Society.

3.2.2. SMOSC-based UV phototransistors

J-aggregated organic semiconductors of 1,3,6,8-tetrakis((4-hexyl phenyl)ethynyl)pyrene(PY-4(THB)) were developed by Choi's group to detect 400 nm light.[43] In its single-crystalline microribbon, PY-4(THB) had face-on aggregated pyrene cores which were favorable for charge transport. The PY-4(THB) microribbon-based OPTs exhibited a high field-effect mobility of 0.7 cm^2·V^{-1}·s^{-1} with a R of 2000 A·W^{-1} under quite low light intensity of 5.6 μW·cm^{-2}. Microplates of anthracene derivative consisting of phenyl planes and acetylene groups were reported by Kim *et al.*[44] The microplate-based OPT had a quite high R of 1.1×10^4 A·W^{-1} and a champion photoswitching ra-

tio of 1.4×10^5 among single-crystalline microplate-based OPTs. In recent years, concerns have focused on pure-UV detectors with visible-blind response. Well-aligned 2,7-dioctyl[1]benzothieno[3,2-b][1]benzothiophene (C8-BTBT) nanoribbon arrays (Fig. 7(a))[45] and naphthalene diimides (NDIs) single nanoribbon (Fig. 7(b))[46] have been fabricated to construct deep-UV OPTs. The photoresponse of the C8-BTBT nanoribbon-based device is shown in Fig. 7(c), which showed obvious response under UV lights of 280 nm and 365 nm. Instead, when visible light was used, almost no difference could be found between the transfer curves with light turned on and off. The absorption spectrum in Fig. 7(d) further indicated the visible light transparent feature of C8-BTBT, the C8-BTBT nanoribbons are thus promising for pure-UV detection. In the case of NDI derivatives, the nanoribbon phase showed an enhanced UV absorption compared to thin film and solution (Fig. 7(e)), which was caused by phase transition towards enhanced molecular packing order. The device was then illuminated under different wavelengths of light with a constant intensity of 100 $\mu W \cdot cm^{-2}$ (Fig. 7(f)), which showed a sharp photocurrent increase with wavelengths under 450 nm both in photoconductor mode ($V_G = 0$ V) and phototransistor mode ($V_G = 20$ V). Under 365 nm UV light, the device had a maximum R of 7.2×10^3 $A \cdot W^{-1}$ with an ultrahigh detectivity of 3.1×10^{15} Jones, the D^* value is one of the highest values among organic photodetectors.

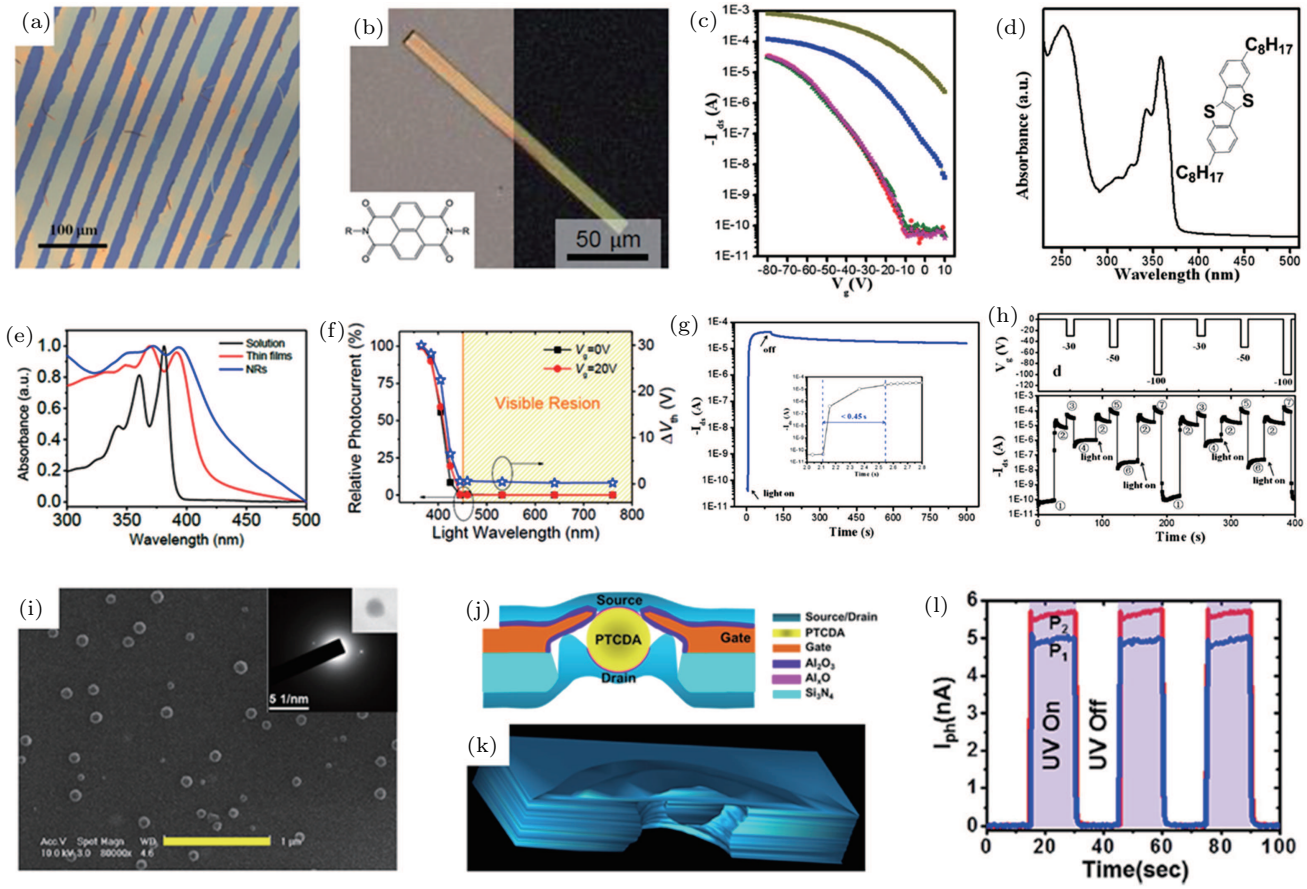


Fig. 7. (a), (b) Optical microscopy images of C8-BTBT nanoribbon arrays and a single NDI nanoribbon, respectively. (c) Transfer characteristics of the C8-BTBT device ($V_{SD} = -30$ V) in dark condition (red curve) and under the illumination of 280 nm (blue curve), 365 nm (yellow curve), 405 nm (magenta curve), and visible light (green curve). (d), (e) Absorption spectra of C8-BTBT crystals and NDI derivatives in different phases, respectively. (f) Relative photocurrent and threshold voltage change of OPTs based on NDI derivatives under the illumination of light with different wavelengths. (b), (e), (f) Reproduced with permission.[46] Copyright 2018, American Chemical Society. (g) Light on/off characteristics of the C8-BTBT device, the inset indicates the rise time of the device. (h) Multiple-stage modulation of I_{DS} by changing the gate bias: ① light-on, ② light-off, ③ $V_G = -30$ V, ④ $V_G = 0$ V, ⑤ $V_G = -50$ V, ⑥ $V_G = 0$ V, ⑦ $V_G = -100$ V. (a), (c), (d), (g), (h) Reproduced with permission.[45] Copyright 2015, Wiley-VCH. (i) SEM image of PTCDA nanoparticles. Inset: SAED pattern of a PTCDA nanoparticle. (j) Schematic illustration of a single PTCDA nanoparticle-based OPT. (k) Three-dimensional (3D) transmission electron microscopy (TEM) tomography image of the nanoparticle device. (l) Photoswitching behavior of the nanoparticle device with different UV intensities: $P_1 = 1.32$ $mW \cdot cm^{-2}$ (blue curve), $P_2 = 2.24$ $mW \cdot cm^{-2}$ (red curve). (i)–(l) Reproduced with permission.[48] Copyright 2013, AIP Publishing.

It is noteworthy that the photomemory phenomenon was observed in the C8-BTBT nanoribbon-based phototransistors.[45] The photoswitching behavior of C8-BTBT at zero gate bias is shown in Fig. 7(g), and the inset indicated a rise time of ~ 0.45 s upon UV light illumination. However, when UV light was turned off, the device showed a persistent current, which was $\sim 10^5$ larger than the previous dark current. The device was then applied as a simple memory unit. As shown in Fig. 7(h), the first step was the light-on process, which could be considered as "writing", the second

light-off step was the "reading" process, in the third/fourth step, V_G was turned from 0 V to $-30/-50$ V and then to 0 V rapidly, which represented the "rereading and rewriting", finally in the "erasing" process, a quite large $V_G = -90$ V was applied, and the off-state current recovered to the initial level. An appropriate explanation is that for p-channel OPTs, after the generation of photo-induced carriers, holes drift toward the conductive channel, while most of electrons are trapped. When no V_G is applied, the trapped electrons can function as the negative gate voltage, causing a persistent increase of source-drain current (I_{SD}). Once V_G with negative bias is applied, I_{SD} increases rapidly due to more accumulation of holes at the insulator/semiconductor interface. Meanwhile, the recombination rate of electrons and holes increases with the increase in the absolute value of V_G, leading to a decrease in I_{SD} when the negative V_G is turned off. Trials have also been done to avoid trapping of electrons in p-type SMOSCs. Mathews *et al.*[47] applied a 600 μs pulsed laser to a rubrene-based OPT, which did not allow enough time for electrons to move into the bulk, and thus led to a fast recombination rate. Instead of the normal long photomemory that persisted for 2 min, a quite short photocurrent decay time of 100 μs was obtained.

Besides conventional OPTs based on 1D and 2D nanostructures, the UV response behavior of single-crystalline nanoparticles has been studied by Nguyen *et al.*[48] Perylene tetracarboxylic dianhydride (PTCDA) nanoparticles with diameters of ∼ 80 nm (Fig. 7(i)) were deposited onto a Si_3N_4 membrane through a simple thermal evaporation process. The selected area electron diffraction (SAED) pattern (inset of Fig. 7(i)) indicated the single-crystalline nature of PTCDA nanoparticles. Novel nanoparticle-based OPTs were constructed by growing PTCDA nanoparticles inside bowl-shaped pores on Si_3N_4 and depositing volcano-shaped Al gate electrodes with Al_2O_3 insulating layers (Figs. 7(j) and 7(k)). The device showed stable switching behavior with increasing UV light intensity (Fig. 7(l)), and the EQE reached a high value of 3.5×10^6%. The single nanoparticle device was thus able to reveal the intrinsic properties of SMOSCs without the influence of grain boundaries.

3.2.3. NIR and broadband phototransistors

The existence of many applications of highly sensitive NIR photodetectors in the field of remote control, fire and airborne early warning, and biomedicine, pushed the development of NIR phototransistors.[27–29] Recently, novel NIR OPTs based on ultrathin SMOSCs have been reported by Wang and coworkers.[49] 2D single-crystalline films based on

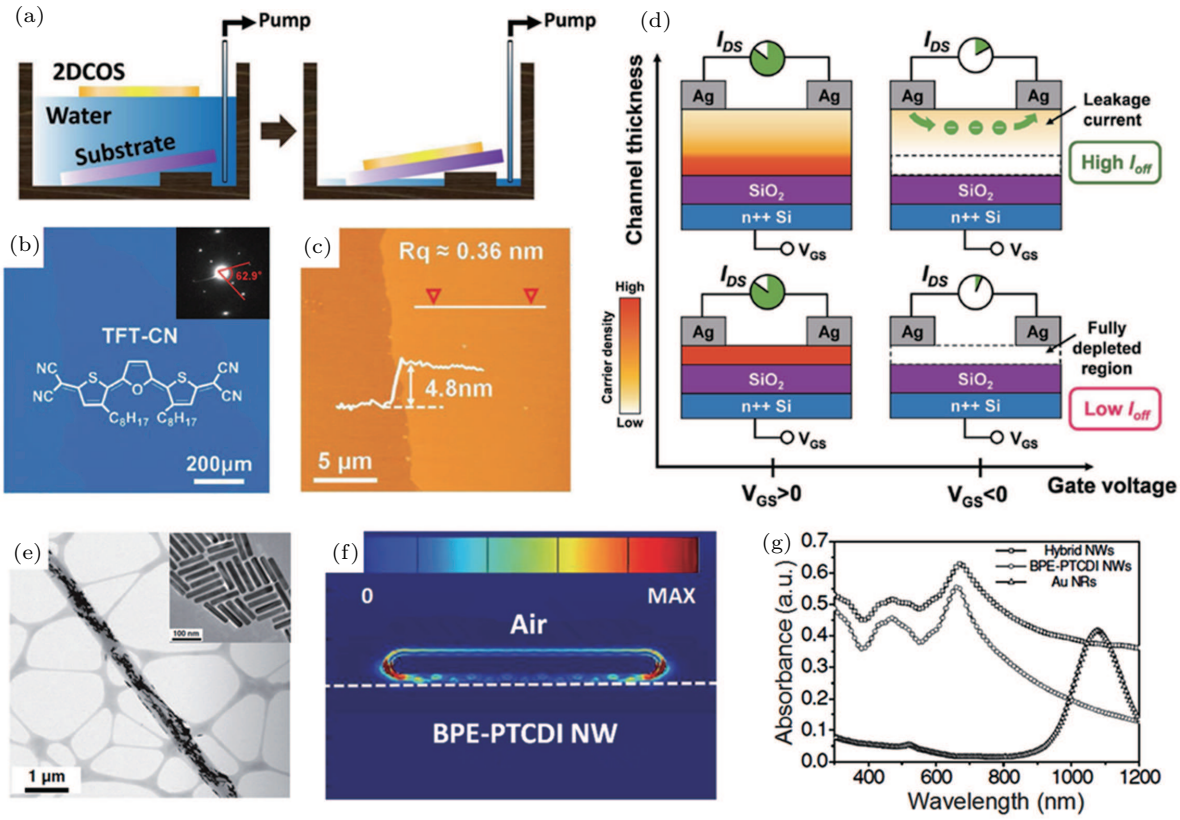


Fig. 8. (a) Schematic illustration of transferring 2D TFT-CN films onto an arbitrary substrate. (b) Optical microscopy image of a TFT-CN film, the inset is the corresponding SAED pattern. (c) Atomic force microscopy (AFM) image of a TFT-CN film with an average roughness of ∼ 0.36 nm and thickness of ∼ 4.8 nm. (d) Schematic diagram of OPTs with different active layer thicknesses under different V_G in dark. (a)–(d) Reproduced with permission.[49] Copyright 2018, Wiley-VCH. (e) High-resolution transmission electron microscopy (HRTEM) image of a hybrid BPE-PTCDI nanowire. Inset: TEM image of Au nanorods. (f) FDTD simulation of the electric field enhancement in a hybrid BPE-PTCDI nanowire under 980 nm light. (g) Absorption spectra of BPE-PTCDI nanowires, Au nanorods, and a hybrid BPE-PTCDI nanowire dispersion in ethanol. (e)–(g) Reproduced with permission.[50] Copyright 2016, Wiley-VCH.

a furan-thiophene quinoidal compound called TFT-CN were fabricated successfully on water surface (Fig. 8(a)). The single-crystalline TFT-CN films had an average thickness of 4.8 nm in a large area of around 10×20 μm^2 (Figs. 8(b) and 8(c)), which was ideal building block for high-performance OPTs. As illustrated in Fig. 8(d), the left figures represent the accumulation regime. In thicker SMOSCs, there is a gradient of the carrier density from the electrodes to the gate dielectric. However, for ultrathin films, the carrier density remains almost constant. The right figures are of the depletion regime, where only ultrathin films are fully depleted, which means that rare leakage current exists. Therefore, the as-prepared TFT-CN ultrathin film OPTs had a quite low dark current of 0.3 pA with an ultrahigh D^* of 6×10^{14} Jones under 808 nm NIR light. Moreover, the EQE reached 4×10^6% along with a high R of 9×10^4 A·W^{-1}, showing the great application potential in NIR detection. In order to enlarge the detection range of SMOSC-based photodetectors, hybrid phototransistors were constructed by combining BPE-PTCDI single crystals with Au nanorods (Fig. 8(e)).[50] As simulated by finite difference time domain (FDTD) in Fig. 8(f), with the existence of light-scattering plasmonic Au nanorods, the electric field around Au surface was intensified under NIR light and additional hot electrons could be injected into the adjacent BPE-PTCDI nanowires upon light illumination. As a result, the hybrid phototransistor was capable of wide-spectrum detection from 350 nm to 980 nm (Fig. 8(g)). A maximum R of 7.7×10^5 A·W^{-1} with a maximum EQE of 1.42×10^8% was obtained under 2.5 μW·cm^{-2} red light. The hybrid system demonstrated a feasible way to construct high-performance and broadband photodetectors, however, the major shortcoming was the quite slow response speed of several seconds.

3.3. SMOSC-based photodiodes

Photodiodes rely on a built-in electric field to separate excitons, providing an efficient separation and a fast collection of photogenerated charge carriers.[5] For organic photodiodes based on SMOSCs, the common configurations include all SMOSC-based p–n junctions, Schottky junctions, and organic/inorganic heterojunctions. The three types of devices will be discussed in this section.

3.3.1. All SMOSC-based p–n junctions

A breakthrough of fabricating p–n junctions constructed by all SMOSCs was made by Zhang and coworkers in 2010.[51] Bilayer nanoribbons consisting of p-type CuPc and n-type copper hexadecafluorophthalocyanine (F_{16}CuPc) were successfully fabricated by using a two-step PVD method. The two kinds of SMOSCs are similar in molecular structure and lattice constants, ensuring highly selective crystallization (Figs. 9(a)–9(d)). Then photodiodes were constructed by depositing asymmetric Au and Al electrodes at two sides of the nanoribbons, a pronounced photocurrent was observed at AM 1.5. Core-shell coaxial p–n junctions (Fig. 9(e)) consisting of p-type CuPc and n-type 5,10,15,20-tetra(4-pyridyl)-porphyrin (H_2TPyP) nanowires were fabricated by Cui *et al.*[52] The p–n junction device (Fig. 9(f)) had a photoswitching ratio of around 100 when white light with an intensity of 5.51 mW·cm^{-2} was turned on and off, and the performance was better than that of each single component device. Instead of the PVD method, Park *et al.*[53] reported the fabrication of cross-stacked organic p–n junctions via solution-based transfer printing for the first time. The detailed process is shown in Fig. 9(g), where electron beam lithography (EBL) was used to pattern nanolines down to 100 nm in width onto a polyurethane acrylate (PUA) mold. The PUA mold was then coated with C_{60} ink solution to form C_{60} nanowires in channels. After contact printing, C_{60} nanowires could be transferred from the mold to a flexible poly(ethersulfone) (PES) substrate. With the consecutive alignment and contact printing of 6,13-bis-(triisopropylsilylethynyl) pentacene (TIPS-PEN) nanowires, cross-aligned single-crystalline C_{60}/TIPS-PEN heterojunctions were formed (Figs. 9(h) and 9(i)). The single heterojunction device showed diode characteristics with a rectification ratio of 13.5 at 50 V. However, due to the small junction area ($\sim 1 \times 10^{-10}$ cm^2), the photoresponse was quite poor. In order to improve the poor device performance caused by small junction area, single-crystalline 2D layered heterojunctions were fabricated by Wang's group.[54] It was found that C8-BTBT (or PTCDA) molecules tend to epitaxially grow on graphene substrate to form a uniform monolayer ($\sim$ 0.9 nm) in a PVD process (Figs. 9(j)–9(k)). Heterojunction photodetectors with vertically stacked Au/C_8-BTBT/PTCDA/graphene structures were thus constructed (Fig. 9(l)), which showed ideal diode characteristics with a rectification ratio of over 10^3 (Fig. 9(m)). Under 514 nm light illumination, a R of 0.37 mA·W^{-1} was obtained.

3.3.2. Schottky junctions and organic/inorganic heterojunctions

Besides all SMOSC-based p–n junction photodiodes, single-crystalline organic semiconductor/metal Schottky junction photodiodes and organic/inorganic semiconductor p–n junction photodiodes have also been reported so far. Jie's group[55] reported the *in situ* self-assembly of 2,4-bis[4-(N, N-dimethylamino)phenyl]squaraine (SQ) nanowire arrays directly on a SiO_2/Si substrate with pre-deposited Au/Ti electrodes (Fig. 10(a)). Schottky-type photodetectors (Fig. 10(b))

were constructed due to the large work function difference between SQ nanowires and the Ti electrode (Fig. 10(c)). Under white light illumination, the Schottky-type device exhibited obvious rectification behavior with a photoswitching ratio 60 times higher than that of the ohmic-type device. The integrated photodiodes showed uniform rectification characteristics with small pixel-to-pixel variation under 0.1 mW·cm^{-2} white light (Figs. 10(d) and 10(e)). The applications of self-assembled SQ nanowires were further broadened by the same group.[56] SQ solution was dropped onto a crystalline Si (c-Si) substrate with pre-patterned SiO_2 layer and Au electrodes (Fig. 10(f)). The device took the advantages of both organic SQ nanowires and inorganic c-Si, leading to a high rectification ratio of 10^4 as well as the broadband photoresponse from UV to NIR. It is noteworthy that the photoresponse within the detection wavelength range was quite even with R values greater than 1 A·W^{-1} and D^* values greater than 6×10^9 Jones (Fig. 10(g)), the R (1.3–9.8 A·W^{-1}) was much better than those of organic heterojunction broadband photodetectors.[57,58] Recently, Wang and coworkers[54,59] have reported the optoelectronic applications of 2D C8-BTBT single crystals by van der Waals epitaxial growth. Due to the relatively strong van der Waals interactions between the deposited organic layers and the 2D atomic crystal substrates (such as graphene, BN, and MoS_2), ordered molecular packing can occur near the interface without lattice mismatch. Few layers of C8-BTBT crystals were then deposited onto MoS_2 substrate via van der Waals epitaxial growth.[59] A R of 22 mA·W^{-1} under white light at zero bias was obtained, along with a power conversion efficiency of 0.31%, paving the way for organic/inorganic self-driven photodetectors.

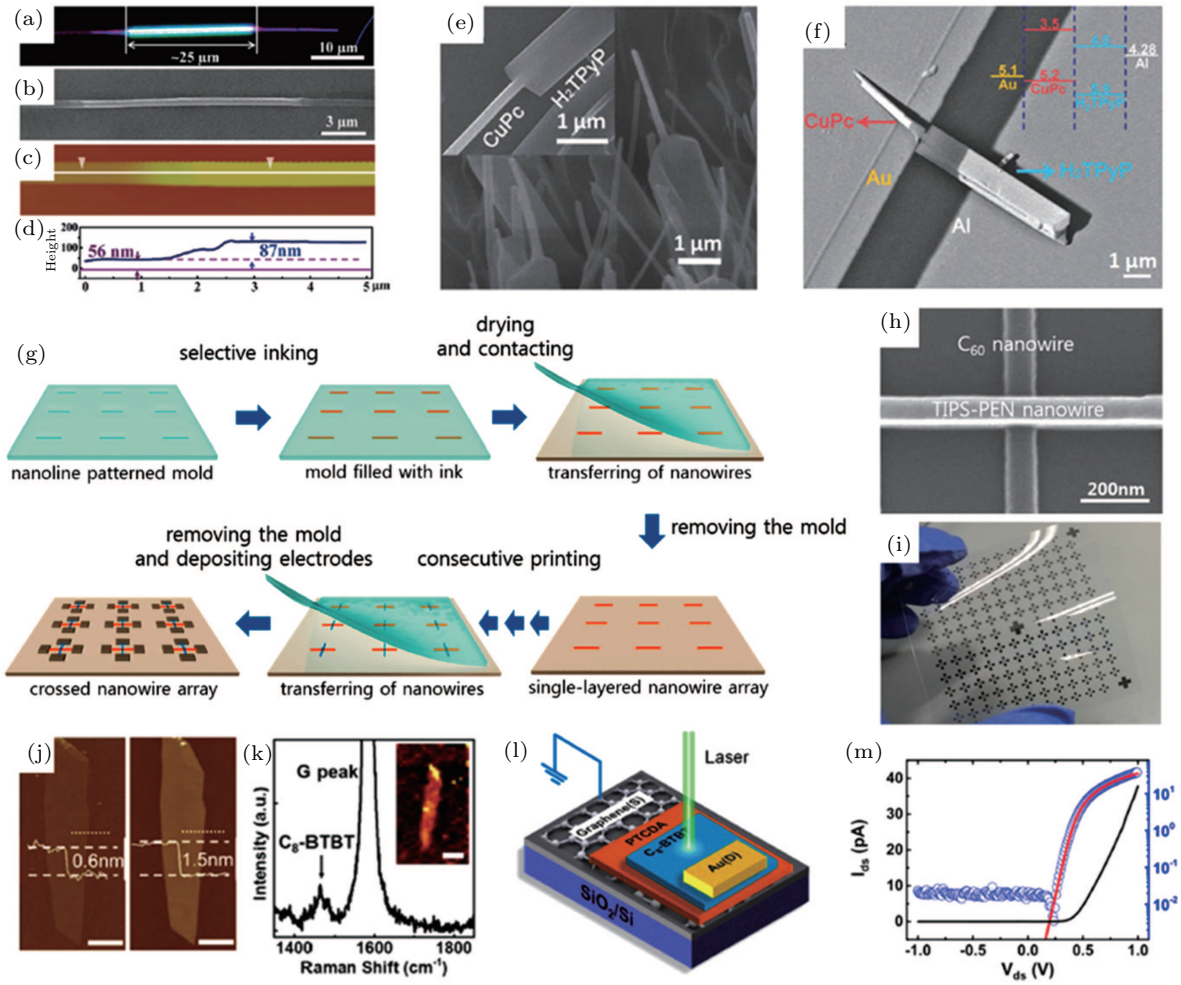


Fig. 9. (a)–(d) Optical, SEM, AFM characterizations and the height profile of a CuPc/F_{16}CuPc p–n junction nanowire, respectively. (a)–(d) Reproduced with permission.[51] Copyright 2010, American Chemical Society. (e), (f) SEM images of the CuPc/H_2TPyP p–n junction and the corresponding device, respectively. (e), (f) Reproduced with permission.[52] Copyright 2012, Wiley-VCH. (g) Schematic illustration of the transfer and patterning procedure for the fabrication of cross-stacked organic p–n junctions. (h) SEM image of the cross-stacked C_{60}/TIPS-PEN p–n junction. (i) Photograph of integrated C_{60}/TIPS-PEN photodiodes on a flexible substrate. (g)–(i) Reproduced with permission.[53] Copyright 2014, American Chemical Society. (j) AFM images of a graphene layer before (left) and after (right) epitaxial growth of C8-BTBT. Scale bar: 2 μm. (k) Raman spectrum of the C8-BTBT layer grown on graphene. Inset: Raman mapping of the C8-BTBT signal. Scale bar: 2 μm. (l) The device structure illustration of a PTCDA/C8-BTBT p–n junction photodiode. (m) I–V characteristics of the PTCDA/C8-BTBT p–n junction in linear scale (black) and log scale (blue), the red line is the fitting curve of a standard diode. (j)–(m) Reproduced with permission.[54] Copyright 2016, American Chemical Society.

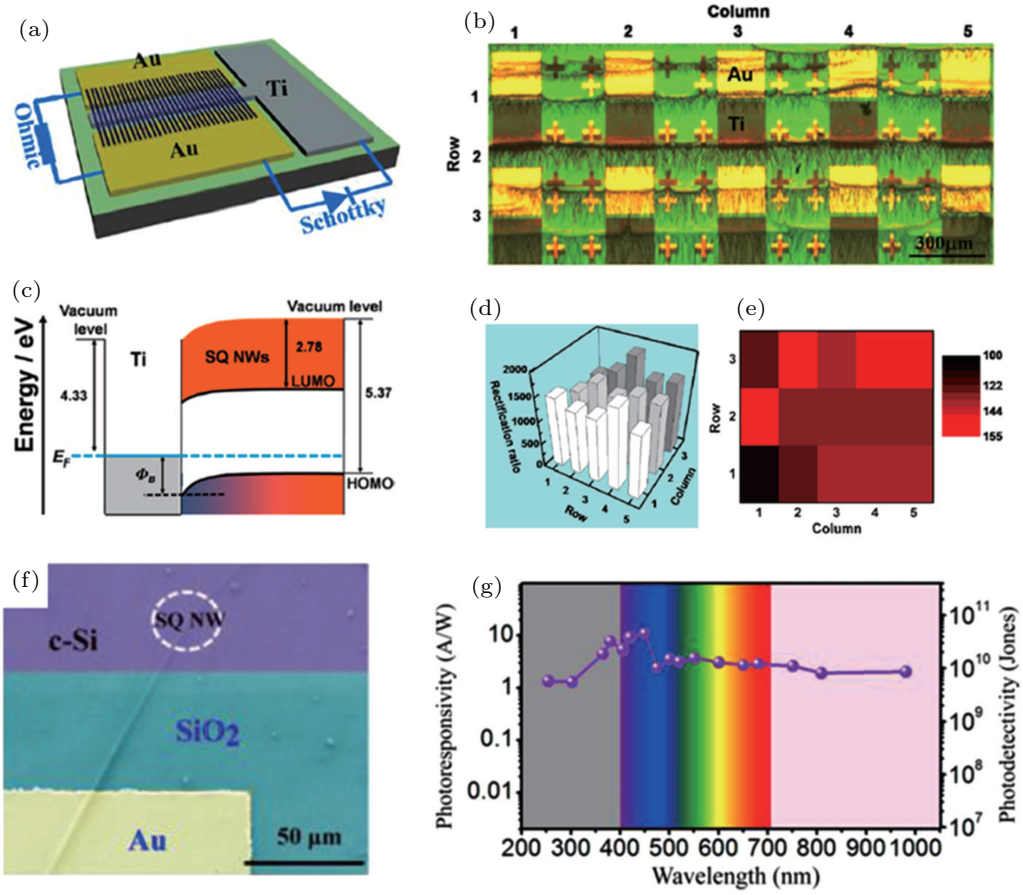


Fig. 10. (a) Schematic illustration of an SQ nanowires/Ti Schottky photodiode. (b) Optical microscopy image of the integrated SQ nanowires/Ti Schottky photodiode. (c) Energy band diagram of the SQ nanowires/Ti Schottky junction. (d) Distribution of the rectification ratio for each Schottky-type device in dark. (e) 2D contrast map of the integrated Schottky-type photodiode under 0.1 mW·cm^{-2} white light. (a)–(e) Reproduced with permission.[55] Copyright 2013, American Chemical Society. (f) SEM image of a single SQ nanowire/c-Si device. (g) Wavelength-dependent R and D^* of the SQ nanowire/c-Si device. (f), (g) Reproduced with permission.[56] Copyright 2014, American Chemical Society.

4. Summary and outlook

In summary, SMOSCs with low defect density and few grain boundaries provide an efficient way for charge transport, and a diversity of SMOSCs brings about broadband light absorption from UV to NIR. Therefore, they are promising candidates for high-performance photodetectors. Over the past few decades, different types of SMOSC-based photodetectors, such as photoconductors, phototransistors, and photodiodes, have been successfully achieved, and the device performances have been significantly improved. As summarized in Table 1, the best figure-of-merit parameters of SMOSC-based photodetectors reported to date, which include high R exceeding 7.7×10^5 A·W^{-1},[48] high D^* approaching 3.1×10^{15} Jones,[46] large photoswitching ratio of 1.9×10^6,[50] and short response time of $\sim$0.1 ms,[47] can be used across a wide range of application domains.

Despite the great progresses of SMOSC-based photodetectors that have been achieved in recent years, there are many challenges left in this field. (i) The response speed needs to be further enhanced to meet the requirements for practical applications. Currently, the response times of most of SMOSC-based photodetectors remain tens or hundreds of milliseconds, which are not enough to capture videos. (ii) The current developed SMOSC-based photodetectors have a very weak sensitivity to infrared light. Although narrow-bandgap conjugated organic semiconductors can be obtained through chemical synthesis, the resulting compounds are unstable in air. Therefore, device encapsulation is necessary to enhance the stability of infrared light detectors. Also, novel hybrid device structures utilizing plasmonic technologies can be employed to improve infrared light detection. (iii) Although the applications of SMOSC-based photodetectors in image sensors have been demonstrated, the image resolution needs to be further improved and the commercialization still remains difficult to realize. This is mainly because the integration of SMOSC-based photodetectors is not compatible with the conventional complementary metal-oxide-semiconductor (CMOS) technologies. Therefore, further development of high-performance photodetectors based on SMOSCs is a long-term challenge.

Table 1. Device performances of the present SMOSC-based photodetectors with three different structures: photoconductors (OPCs), phototransistors (OPTs), and photodiodes (OPDs).

Type	Material	λ/nm	R/A·W^{-1}	D^*/Jones	Photoswitching ratio	t/ms	Ref.
OPC	Porphine derivative	488	N/A	N/A	N/A	100	[9]
OPC	Anthracene derivative	white light	N/A	N/A	10^2	N/A	[14]
OPC	Benzothiophene	405	4.2×10^2	N/A	10^3	N/A	[15]
OPC	Benzothiophene	405	4.4×10^3	N/A	10^4	N/A	[16]
OPC	CuPc	650	N/A	N/A	180	100	[18]
OPC	Alq3	254	14.5	2.0×10^{12}	N/A	N/A	[25]
OPC	C_{60}	400	8.0×10^{-3}	7.1×10^8	365	1800	[26]
OPC	MeSq	500–700	N/A	N/A	10^3	N/A	[31]
OPC	MeSq	808	N/A	N/A	1.6×10^3	1400	[33]
OPC	F_{16}CuPc	589–940	6.0×10^{-5}	N/A	300	400	[60]
OPT	TTF derivative	white light	N/A	N/A	10^4	N/A	[34]
OPT	BPEA	white light	N/A	N/A	6.0×10^3	N/A	[35]
OPT	Me-ABT	white light	1.2×10^4	N/A	6.0×10^3	N/A	[36]
OPT	BPE-PTCDI	532–680	1.4×10^3	N/A	5.0×10^3	N/A	[37]
OPT	C_{70}−DPTTA	white light	3.0×10^2	N/A	N/A	N/A	[39]
OPT	TCNQ	white light	1.0×10^{-3}	N/A	31	10	[40]
OPT	PTCDI-C8	white light	7	N/A	2.5×10^3	N/A	[41]
OPT	PTCDI-C8	500	4.8×10^4	N/A	2.9×10^4	N/A	[42]
OPT	PY-4(THB)	400	2.0×10^4	N/A	1.2×10^6	N/A	[43]
OPT	Anthracene derivative	400	1.1×10^4	N/A	1.4×10^5	N/A	[44]
OPT	C8-BTBT	280–365	8.0×10^3	N/A	1.1×10^6	450	[45]
OPT	NDI-PM	365	7.2×10^3	3.1×10^{15}	2.0×10^5	400	[46]
OPT	Rubrene	405	2.7×10^3	N/A	N/A	0.1	[47]
OPT	TFT-CN	808	9.0×10^4	6.0×10^{14}	5.0×10^5	N/A	[49]
OPT	BPE-PTCDI	350–980	7.7×10^5	N/A	1.9×10^6	1500	[50]
OPT	F_{16}CuPc	white light	N/A	N/A	4.5×10^4	10	[61]
OPT	TCNQ	white light	N/A	N/A	160	500	[62]
OPD	CuPc/H_2TPyP	white light	N/A	N/A	10^2	N/A	[52]
OPD	C8-BTBT/PTCDA	514	3.7×10^{-4}	N/A	N/A	N/A	[54]
OPD	SQ/Ti	white light	N/A	N/A	10^2	300	[55]
OPD	SQ/Si	254–980	9.8	4.5×10^{10}	979	600	[56]
OPD	C8-BTBT/MoS_2	white light	2.2×10^{-2}	N/A	N/A	N/A	[59]

References

[1] Zhang X J, Jie J S, Deng W, Shang Q X, Wang J C, Wang H, Chen X F and Zhang X H 2016 *Adv. Mater.* **28** 2475
[2] Reese C and Bao Z N 2007 *Mater. Today* **10** 20
[3] Deng W, Zhang X J, Dong H L, Jie J S, Xu X Z, Liu J, He L, Xu L, Hu W P and Zhang X H 2018 *Mater. Today* in press
[4] Deng W, Zhang X J, Wang L, Wang J C, Shang Q X, Zhang X H, Huang L M and Jie J S 2015 *Adv. Mater.* **27** 7305
[5] Baeg K J, Binda M, Natali D, Caironi M and Noh Y Y 2013 *Adv. Mater.* **25** 4267
[6] Dong H L, Zhu H F, Meng Q, Gong X and Hu W P 2012 *Chem. Soc. Rev.* **41** 1754
[7] Pierre1 A and Arias A C 2016 *Flex. Print. Electron.* **1** 043001
[8] Wang H L, Liu H T, Zhao Q, Ni Z J, Zou Y, Yang J, Wang L F, Sun Y Q, Guo Y L, Hu W P and Liu Y Q 2017 *Adv. Mater.* **29** 1701772
[9] Schwab A D, Smith D E, Bond-Watts B, Johnston D E, Hone J, Johnson A T, de Paula J C and Smith W F 2004 *Nano Lett.* **4** 1261
[10] Deng W, Zhang X J, Zhang X H, Guo J H and Jie J S 2017 *Adv. Mater. Technol.* **2** 1600280
[11] Deng W, Huang L M, Xu X Z, Zhang X J, Jin X C, Lee S T and Jie J S 2017 *Nano Lett.* **17** 2482
[12] Xie C, Mak C, Tao X M and Yan F 2017 *Adv. Funct. Mater.* **27** 1603886
[13] Wang C L, Dong H L, Jiang L and Hu W P 2018 *Chem. Soc. Rev.* **47** 422
[14] Jiang L, Fu Y Y, Li H X and Hu W P 2008 *J. Am. Chem. Soc.* **130** 3937
[15] Zhou Y, Wang L, Wang J, Pei J and Cao Y 2008 *Adv. Mater.* **20** 3745
[16] Ai N, Zhou Y, Zheng Y N, Chen H B, Wang J, Pei J and Cao Y 2013 *Org. Electron.* **14** 1103
[17] Zhang Y P, Wang X D, Wu Y M, Jie J S, Zhang X W, Xing Y L, Wu H H, Zou B, Zhang X J and Zhang X H 2012 *J. Mater. Chem.* **22** 14357
[18] Wu Y M, Zhang X J, Pan H H, Zhang X W, Zhang Y P, Zhang X Z and Jie J S 2013 *Nanotechnology* **24** 355201
[19] Wu Y M, Zhang X J, Pan H H, Deng W, Zhang X H, Zhang X W and Jie J S 2013 *Sci. Rep.* **3** 3248
[20] Deng W, Zhang X J, Huang L M, Xu X Z, Wang L, Wang J C, Shang Q X, Lee S T and Jie J S 2016 *Adv. Mater.* **28** 2201
[21] Zou Y A, Zhang Y, Hu Y M and Gu H S 2018 *Sensors* **18** 2072
[22] Sun B, Sun Y and Wang C X 2018 *Small* **14** 1703391
[23] Bie Y Q, Liao Z M, Zhang H Z, Li G R, Ye Y, Zhou Y B, Xu J, Qin Z X, Dai L and Yu D P 2011 *Adv. Mater.* **23** 649
[24] Wei M S, Yao K Y, Liu Y M, Yang C, Zang X N and Lin L W 2017 *Small* **13** 1701328
[25] Zhang Y D, Jie J S, Sun Y N, Jeon S G, Zhang X J, Dai G L, Lee C J and Zhang X H 2017 *Small* **13** 1604261
[26] Zheng S S, Xiong X, Zheng Z, Xu T, Zhang L, Zhai T Y and Lu X 2018 *Carbon* **126** 299
[27] Kataria M, Yadav K, Cai S Y, Liao Y M, Lin H I, Shen T L, Chen Y H, Chen Y T, Wang W H and Chen Y F 2018 *ACS Nano* **12** 9596
[28] Zeng L H, Xie C, Tao L L, Long H, Tang C Y, Tsang Y H and Jie J S 2015 *Opt. Express* **23** 4839
[29] Song J, Qu J, Swihart M T and Prasad P N 2016 *Nanomed. Nanotechnol. Bio. Med.* **12** 771
[30] Chen H Y, Liu H, Zhang Z M, Hu K and Fang X S 2016 *Adv. Mater.* **28** 403
[31] Zhang X J, Jie J S, Zhang W F, Zhang C Y, Luo L B, He Z B, Zhang X H, Zhang W J, Lee C S and Lee S T 2008 *Adv. Mater.* **20** 2427
[32] Xing Y L, Deng W, Wang H, Gong C, Zhang X J and Jie J S 2015 *J. Nanosci. Nanotechnol.* **15** 4450
[33] Wang H, Deng W, Huang L M, Zhang X J and Jie J S 2016 *ACS Appl. Mater. Inter.* **8** 7912

[34] Mas-Torrent M, Hadley P, Crivillers N, Veciana J and Rovira C 2006 *ChemPhysChem* **7** 86
[35] Wang C L, Liu Y L, Wei Z M, Li H X, Xu W and Hu W P 2010 *Appl. Phys. Lett.* **96** 143302
[36] Guo Y L, Du C Y, Yu G, Di C A, Jiang S D, Xi H X, Zheng J, Yan S K, Yu C L, Hu W P and Liu Y Q 2010 *Adv. Funct. Mater.* **20** 1019
[37] Yu H, Bao Z A and Oh J H 2013 *Adv. Funct. Mater.* **23** 629
[38] Johnson N M and Chiang A 1984 *Appl. Phys. Lett.* **45** 1102
[39] Zhang J, Tan J H, Ma Z Y, Xu W, Zhao G Y, Geng H, Di C A, Hu W P, Shuai Z G, Singh K and Zhu D B 2013 *J. Am. Chem. Soc.* **135** 558
[40] Mukherjee B, Mukherjee M, Sim K and Pyo S 2011 *J. Mater. Chem.* **21** 1931
[41] Mukherjee B, Sim K, Shin T J, Lee J, Mukherjee M, Ree M and Pyo S 2012 *J. Mater. Chem.* **22** 3192
[42] Yao Y F, Zhang L, Leydecker T and Samori P 2018 *J. Am. Chem. Soc.* **140** 6984
[43] Kim Y S, Bae S Y, Kim K H, Lee T W, Hur J A, Hoang M H, Cho M J, Kim S J, Kim Y, Kim M, Lee K, Lee S J and Choi D H 2011 *Chem. Commun.* **47** 8907
[44] Kim K H, Bae S Y, Kim Y S, Hur J A, Hoang M H, Lee T W, Cho M J, Kim Y, Kim M, Jin J I, Kim S J, Lee K, Lee S J and Choi D H 2011 *Adv. Mater.* **23** 3095
[45] Wu G, Chen C, Liu S, Fan C C, Li H Y and Chen H Z 2015 *Adv. Electron. Mater.* **1** 1500136
[46] Song I, Lee S C, Shang X, Ahn J, Jung H J, Jeong C U, Kim S W, Yoon W, Yung H, Kwon O P and Oh J H 2018 *ACS Appl. Mater. Inter.* **10** 11826
[47] Mathews N, Fichou D, Menard E, Podzorov V and Mhaisalkar S G 2010 *Appl. Phys. Lett.* **97** 212108
[48] Nguyen L N, Pradhan S K, Yen C N, Lin M C, Chen C H, Wu C S, Chang-Liao K S, Lin M T and Chen C D 2013 *Appl. Phys. Lett.* **103** 183301
[49] Wang C, Ren X C, Xu C H, Fu B B, Wang R H, Zhang X T, Li R J, Li H X, Dong H L, Zhen Y G, Lei S B, Jiang L and Hu W P 2018 *Adv. Mater.* **30** 1706260
[50] Jung J H, Yoon M J, Lim J W, Lee Y H, Lee K E, Kim D H and Oh J H 2017 *Adv. Funct. Mater.* **27** 1604528
[51] Zhang Y J, Dong H L, Tang Q X, Ferdous S, Liu F, Mannsfeld S C B, Hu W P and Briseno A L 2010 *J. Am. Chem. Soc.* **132** 11580
[52] Cui Q H, Jiang L, Zhang C, Zhao Y S, Hu W P and Yao J N 2012 *Adv. Mater.* **24** 2332
[53] Park K S, Lee K S, Kang C M, Baek J, Han K S, Lee C, Lee Y E K, Kang Y and Sung M M 2015 *Nano Lett.* **15** 289
[54] Wu B, Zhao Y H, Nan H Y, Yang Z Y, Zhang Y H, Zhao H J, He D W, Jiang Z L, Liu X L, Li Y, Shi Y, Ni Z H, Wang J L, Xu J B and Wang X R 2016 *Nano Lett.* **16** 3754
[55] Zhang Y P, Deng W, Zhang X J, Zhang X W, Zhang X H, Xing Y L and Jie J S 2013 *ACS Appl. Mater. Inter.* **5** 12288
[56] Deng W, Jie J S, Shang Q X, Wang J C, Zhang X J, Yao S W, Zhang Q and Zhang X H 2015 *ACS Appl. Mater. Inter.* **7** 2039
[57] Gong X, Tong M H, Xia Y J, Cai W Z, Moon J S, Cao Y, Yu G, Shieh C L, Nilsson B and Heeger A J 2009 *Science* **325** 1665
[58] Xie Y, Gong M G, Shastry T A, Lohrman J, Hersam M C and Ren S Q 2013 *Adv. Mater.* **25** 3433
[59] He D W, Pan Y M, Nan H Y, Gu S A, Yang Z Y, Wu B, Luo X G, Xu B C, Zhang Y H, Li Y, Ni Z H, Wang B G, Zhu J, Chai Y, Shi Y and Wang X R 2015 *Appl. Phys. Lett.* **107** 183103
[60] Zou T Y, Wang X Y, Ju H D, Wu Q, Guo T T, Wu W and Wang H 2018 *J. Mater. Chem. C* **6** 1495
[61] Tang Q X, Li L Q, Song Y B, Liu Y L, Li H X, Xu W, Liu Y Q, Hu W P and Zhu D B 2007 *Adv. Mater.* **19** 2624
[62] Jiang H, Yang X J, Cui Z D, Liu Y C, Li H X and Hu W P 2009 *Appl. Phys. Lett.* **94** 123308